Geophys. J. R. astr. Soc. (1986) **84**, 331–359

Efficient global matrix approach to the computation of synthetic seismograms

Henrik Schmidt *SACLANT ASW Research Centre, Viale San Bartolomeo 400, I-19026 San Bartolomeo (SP), La Spezia, Italy*

Gerard Tango *Naval Ocean Research and Development Activity, NSTL, Mississippi 39529, USA*

Accepted 1985 July 2. Received 1985 June 25; in original form 1985 February 1

Summary. A numerically efficient global matrix approach to the solution of the wave equation in horizontally stratified environments is presented. The field in each layer is expressed as a superposition of the field produced by the sources within the layer and an unknown field satisfying the homogeneous wave equations, both expressed as integral representations in the horizontal wavenumber. The boundary conditions to be satisfied at each interface then yield a linear system of equations in the unknown wavefield amplitudes, to be satisfied at each horizontal wavenumber. As an alternative to the traditional propagator matrix approaches, the solution technique presented here yields both improved efficiency and versatility. Its global nature makes it well suited to problems involving many receivers in range as well as depth and to calculations of both stresses and particle velocities. The global solution technique is developed in close analogy to the finite element method, thereby reducing the number of arithmetic operations to a minimum and making the resulting computer code very efficient in terms of computation time. These features are illustrated by a number of numerical examples from both crustal and exploration seismology.

Key words: integral transforms, matrix methods, reflectivity methods, seismic propagation, stratified media, synthetic seismograms

1 Introduction

The use of integral transform techniques to solve the wave equation in horizontally stratified fluid or solid environments is well established in underwater acoustics and seismology, where it forms the theoretical basis for several numerical propagation models. Pekeris (1948) and later Jardetzky (1953) and Ewing, Jardetzky & Press (1957) treated the problem of propagation in plane layered waveguides using simple two- and three-layered models. The physical displacement and stress quantities in each layer were expressed as integral representations in the horizontal wavenumber resulting from the superposition of an unknown field satisfying the homogeneous wave equations and a forcing term due to a

possible source within the layer. The transform kernels of the unknown field were then found from the boundary conditions to be satisfied at each interface.

For the few-layered cases originally presented, the resulting linear system of equations in the unknown wave amplitudes could easily be solved analytically. For more complicated environmental models, however, this procedure is inconvenient. Before the advent of large digital computers and associated solver software, the Green's function computation has therefore historically been tackled by propagator matrix methods, as introduced into seismology by Thomson (1950) and later variously modified by, for example, Haskell (1953), Harkrider (1964) and Kind (1976, 1978). For many applications propagator matrix techniques has heuristic as well as computational advantages. However, as was realized quite early, in all but the simplest fluid applications, the original propagator matrix requires special numerical treatment, to ensure numerical stability in the evanescent regime for high frequencies and large layer thicknesses, resulting in more time-consuming algorithms. Reviews of these techniques are given by Kennett (1983) and Woodhouse (1981).

The invariant embedding reformulation introduced by Kennett (1974) has the advantage, that individual arrivals can be isolated, but in its original form it was not unconditionably stable. This problem has, however, later been removed by Kennett (1983) and Ha (1984).

Here a more direct, global matrix (DGM) method is taken to the determination of the depth-dependent Green's function. The present technique is in fact a general numerical implementation of the original solution method of Ewing *et al.* (1957), but implemented using efficient numerical techniques adopted from modern finite-element programs.

In what might be termed a direct global matrix or 'finite wave element' approach, the seismic wavefield in each layer is considered as a superposition of the field produced by an arbitrary number of sources and an unknown field satisfying homogeneous wave equations. These unknown fields are then determined from the boundary conditions to be satisfied simultaneously at all layer interfaces. The resulting linear system of equations in the Hankel transforms of the potentials is straightforwardly assembled and written in a global form. The resulting global coefficient matrix is positive definite and block bidiagonal in form, closely analogous to the global stiffness matrix arising in the finite element method. The solution of this global system of equations can therefore be determined efficiently by Gaussian elimination, yielding the field in all layers simultaneously.

A similar global matrix approach has been independently proposed by Chin, Hedstrom & Thigpen (1984), but was not numerically implemented.

Despite the analytic equivalence of local propagator and direct global matrix solutions for the depth-dependent Green's function, there are a number of important advantages of the latter technique for applications to computational seismology:

(1) Any number of sources can be conveniently treated because the fields produced by multiple sources are simply superposed, and no dummy interfaces have to be introduced at the source depths.

(2) Any number of receiver depths can easily be treated, with only one solution pass, since the wavefield potentials are found in all layers simultaneously.

(3) In contrast to the situation for techniques based on propagator matrices, mixed fluid/solid/vacuum cases are readily treated in an efficient manner.

(4) Time-consuming stability assurance problems do not arise, because they are removed automatically by choosing an appropriate coordinate system within each layer together with a proper organization of the global system of equations.

The theoretical basis for seismic wave propagation in a horizontally stratified viscoelastic medium is outlined in Section 2. The numerical solution technique, which is the basis for the

DGM SAFARI code, is described and developed conceptually in formal analogy to the finite element technique in Section 3. To demonstrate the efficiency and versatility of the global solution technique, a series of numerical examples is given in Section 4. First canonical MOHO and LVL problems are treated for comparison with earlier reflectivity results. Crustal tunnelling waves are then modelled in order to demonstrate the ability of the present technique to yield numerically stable solutions in cases where evanescent waves become important. Synthetic vertical seismic profiles are generated for both hypothetical and realistic boreholes, illustrating the efficiency in cases where many receiver depths are considered. Finally, the theoretical completeness of the solution is demonstrated by modelling inhomogeneous S^* arrivals arising from explosive sources close to the surface as well as earthquake sources close to the MOHO.

Applications to propagation problems in underwater acoustics and ultrasonics have been presented by Schmidt (1983, 1984) and Schmidt & Jensen (1984, 1985).

2 Seismic field representation

The representation of the total seismic wavefield in terms of integral solutions here closely follows the presentations given by Ewing *et al.* (1957), Miklowitz (1978) and for the general three-dimensional (3-D) case by Krenk & Schmidt (1982). Thus, only an outline is given here.

The environment is assumed to be a horizontally stratified set of N layers in welded interfacial contact (Fig. 1). All layers, including the upper and lower half-spaces, are considered homogeneous and isotropic viscoelastic continua with Lamé constants λ_m, μ_m and density ρ_m, where the subscript m refers to the layer number.

The field representations are here given in cylindrical coordinates; derivation of the corresponding field representations in plane Cartesian geometry has been given elsewhere (Schmidt & Jensen 1985).

A cylindrical coordinate system $\{r, \theta, z\}$ is introduced, with the z-axis perpendicular to the interfaces and the positive direction being downwards (Fig. 1). The z-axis is chosen to pass through the sources, making the resulting field independent of the azimuthal angle.

The point sources are taken to be harmonic with the angular frequency ω. In complex notation a time dependence of the form $\exp(i\omega t)$ is assumed, a factor that will not be included in the following expressions. Viscoelastic attenuation is accounted for by letting the Lamé constants be complex (e.g. Aki & Richards 1980). In the absence of body forces,

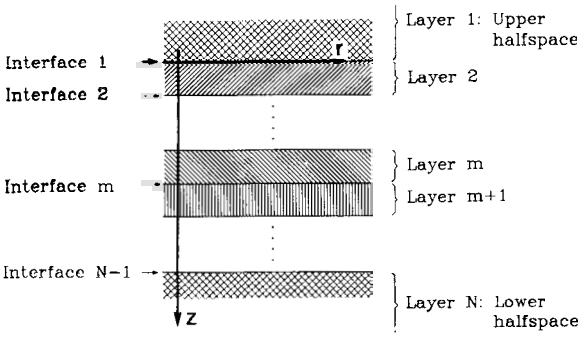

Figure 1. Horizontally stratified environment.

the displacement equations of motion will be satisfied if the displacement components $\{u, w\}$ in each layer m are expressed in terms of the scalar displacement potentials $\{\varphi_m, \psi_m\}$ as

$$u(r, z)|_m = \frac{\partial}{\partial r}\varphi_m + \frac{\partial^2}{\partial r \partial z}\psi_m \tag{1}$$

$$w(r, z)|_m = \frac{\partial}{\partial z}\varphi_m + \frac{1}{r}\frac{\partial}{\partial r} r \frac{\partial}{\partial r}\psi_m \tag{2}$$

where the potentials satisfy the wave equations

$$(\nabla^2 + k_{pm}^2)\varphi_m = 0 \tag{3}$$

$$(\nabla^2 + k_{sm}^2)\psi_m = 0. \tag{4}$$

The constants k_{pm} and k_{sm} are the wavenumbers for compressional and shear waves, respectively. By applying the Hankel transform to (3) and (4) the following integral representations are obtained for the potentials within layer m

$$\varphi_m(r, z) = \int_0^\infty [\![A_m^-(k) \exp[-z\alpha_m(k)] + A_m^+(k) \exp[z\alpha_m(k)]]\!] J_0(kr)\, k\, dk \tag{5}$$

$$\psi_m(r, z) = \int_0^\infty [\![B_m^-(k) \exp[-z\beta_m(k)] + B_m^+(k) \exp[z\beta_m(k)]]\!] J_0(kr)\, dk. \tag{6}$$

Here A_m^-, A_m^+, B_m^- and B_m^+ are arbitrary functions in the horizontal wavenumber k, and

$$\alpha_m(k) = \sqrt{k^2 - k_{pm}^2} \tag{7}$$

$$\beta_m(k) = \sqrt{k^2 - k_{sm}^2}\,. \tag{8}$$

Note that the integrals (5) and (6) above are simply decompositions of the total wavefield into up- and downgoing conical waves, with the arbitrary functions A_m^-, A_m^+, B_m^- and B_m^+ being the amplitudes.

Substitution of (5) and (6) into (1) and (2) gives the following integral representations for the displacement components

$$u(r, z)|_m = \int_0^\infty [-kA_m^- \exp(-z\alpha_m) - kA_m^+ \exp(z\alpha_m) + \beta_m B_m^- \exp(-z\beta_m) - \beta_m B_m^+ \exp(z\beta_m)]\, J_1(kr)\, k\, dk \tag{9}$$

$$w(r, z)|_m = \int_0^\infty [-\alpha_m A_m^- \exp(-z\alpha_m) + \alpha_m A_m^+ \exp(z\alpha_m) + kB_m^- \exp(-z\beta_m) + kB_m^+ \exp(z\beta_m)]\, J_0(kr)\, k\, dk. \tag{10}$$

The corresponding stress components involved in the boundary conditions follow from Hooke's law,

$$\sigma_{zz}(r, z)|_m = \mu_m \int_0^\infty [\![(2k^2 - k_{sm}^2)[A_m^- \exp(-z\alpha_m) + A_m^+ \exp(z\alpha_m)] - 2k\beta_m [B_m^- \exp(-z\beta_m) - B_m \exp(z\beta_m)]]\!] J_0(kr)\, k\, dk \tag{11}$$

$$\sigma_{rz}(r, z)|_m = \mu_m \int_0^\infty [[2k\alpha_m [A_m^- \exp(-z\alpha_m) - A_m^+ \exp(z\alpha_m)]]$$

$$-(2k^2 - k_{sm}^2)\,[B_m^- \exp(-z\beta_m) + B_m^+ \exp(z\beta_m)]\,J_1(kr)\,kdk. \tag{12}$$

To obtain expressions for the total field in a general layer m, the field produced by the source or sources within the layer must be added to the homogeneous solution above. Here only point compressional sources are considered; the field produced by each in an infinite medium with material properties of layer m has the Sommerfeld–Weyl integral representation

$$\overset{*}{\varphi}_m(r, z) = \int_0^\infty \frac{\exp(-|z - z_s|\alpha_m)}{\alpha_m} J_0(kr)\,kdk \tag{13}$$

$$\overset{*}{\psi}_m(r, z) = 0. \tag{14}$$

It should be mentioned, that any source type with integral representations similar to (13) could be used. Several examples are given by Harkrider (1964).

The corresponding displacements involved in the boundary conditions are again obtained from (1) and (2) as

$$\overset{*}{u}(r, z)|_m = -\int_0^\infty \frac{\exp(-|z - z_s|\alpha_m)}{\alpha_m} J_1(kr)\,kdk \tag{15}$$

$$\overset{*}{w}(r, z)|_m = -\int_0^\infty \operatorname{sign}(z - z_s) \exp(-|z - z_s|\alpha_m) J_0(kr)\,kdk \tag{16}$$

while the stresses are likewise obtained from Hooke's law

$$\overset{*}{\sigma}_{zz}(r, z)|_m = \mu_m \int_0^\infty (2k^2 - k_{sm}^2) \frac{\exp(-|z - z_s|\alpha_m)}{\alpha_m} J_0(kr)\,kdk \tag{17}$$

$$\overset{*}{\sigma}_{rz}(r, z)|_m = \mu_m \int_0^\infty 2k \operatorname{sign}(z - z_s) \exp(-|z - z_s|\alpha_m) J_1(kr)\,kdk. \tag{18}$$

If more than one source is present in the mth layer, the kernels of (15)–(18) are simply replaced by a sum over the number sources.

The field at each interface now has two distinct integral representations, one from the layer above and one from the layer below. The boundary conditions of continuity of normal and tangential displacement and stress now have to be satisfied at all ranges r. Thus the boundary conditions must be satisfied by the kernels in the integral representations as well; for the N-layered, free-surface/solid case this leads to a linear system of $4N$-2 equations in the $4N$-2 unknown wavefield amplitudes A_m^-, A_m^+, B_m^-, B_m^+. When this system has been solved, the depth-dependent Green's function follows directly by superposition of the resulting homogeneous solution with the source kernels. The total field in range is then obtained by an evaluation of the integral transforms.

For simple systems comprising only a very limited number of layers, these equations can of course be solved analytically, as done for simple few-layer vacuum/fluid/solid cases by Pekeris (1948) and Ewing *et al.* (1957), but for a more general multilayered environment

this is inconvenient. An efficient and entirely general numerical solution scheme is presented in the following section.

3 Numerical solution by global matrix approach

As in all synthetic seismic methods based on integral transform techniques (e.g. the reflectivity methods of Fuchs & Mueller (1971) and Kennett (1974), the fast field program of Kutschale (1973) and the discrete wavenumber method of Bouchon & Aki (1977)), the numerical solution for the total wavefield problem is divided into two parts. First the depth-dependent Green's function is found at a discrete number of horizontal wavenumbers for the selected receiver depths. Second, the transfer functions are found at all selected depths and ranges by the evaluation of the integral transforms, followed by Fourier synthesis to yield the synthetic seismograms. As seismic experience of over 15 years has shown (e.g. Chapman & Orcutt 1985) the first part – the determination of the depth-dependent Green's function – is by far the most critical in relation to the total computation time, and it is precisely here, in the direct global matrix approach, that the present technique differs in computational approach from recursive local propagator matrix techniques. The emphasis is therefore focused on this first part in the following.

3.1 DEPTH-DEPENDENT GREEN'S FUNCTION

The use of digital computers for numerically solving field problems in continuous media in general requires some kind of discretization. One possibility is to set up the exact field equations for the continuum and subsequently find an approximate solution by discretization of the equations. This is the approach taken in finite difference techniques. The other possibility is to discretize the medium itself and then in effect let the computer numerically determine an exact solution to this now approximate problem.

The best-known example of this latter approach is the finite element method. This technique is based on the division of the continuum into finite blocks or elements connected to each other at a finite number of discrete nodes. Exact local solutions for the single elements, together with the continuity between the elements concentrated in the nodes, lead directly to an exact solution for the approximated global problem. This, however, requires the solution of large linear systems of equations in the unknown degrees of freedom (typically node displacements). The unavailability of sufficient computing power before the last decade delayed the widespread practical use of this powerful technique, which today is the most widely employed methodology in structural mechanics and fluid dynamics, for example.

In this regard, it is easily observed (Schmidt 1984; Schmidt & Jensen 1985) that the integral transform solution of the wave equation for horizontally stratified environments is in the latter 'finite element' catagory. The local expressions for the depth-dependent Green's function are exact within each layer (element), and thus an exact global solution can be obtained directly from the boundary conditions to be satisfied at all interfaces (nodes). It is therefore not surprising that the numerical implementation can be performed in close analogy with the finite element method using efficient numerical tools created within the last decades.

In order to develop this analogy formally, the basic properties of the finite element equations will be briefly outlined at this point. For details reference is made to the pertinent literature (e.g. Zienkiewitz 1977).

The simplest possible static element (Fig. 2a), is chosen as a representative example. It has four degrees of freedom, here the four node displacements $\{u_1, u_2, u_3, u_4\}$. The corresponding node forces are then given by

$$\begin{Bmatrix} p_1 \\ p_2 \\ p_3 \\ p_4 \end{Bmatrix}_m = [k]_m \begin{Bmatrix} u_1 \\ u_2 \\ u_3 \\ u_4 \end{Bmatrix}_m , \quad m = 1, 2 \ldots . N \tag{19}$$

where $[k]_m$ is the local element stiffness matrix, and the subscript refers to the actual element number. As the nodes are in general common to more elements, it is here convenient to introduce a global degree of freedom vector $\{U\}$ defined by

$$\begin{Bmatrix} u_1 \\ u_2 \\ u_3 \\ u_4 \end{Bmatrix}_m = [L]_m \{U\}, \quad m = 1, 2 \ldots . N \tag{20}$$

where $[L]_m$, a topology or connectivity matrix for element m, is an extremely sparse identifier matrix with only four non-vanishing elements equal to unity. The mapping (20) directly reflects the connectivity conditions governing the globally assembled element system in question.

Now Hamilton's principle of stationary energy, together with (19) and (20), leads to the following linear system of equations to be satisfied

$$[K] \{U\} = \{R\}, \tag{21}$$

where $[K]$ is the global stiffness matrix

$$[K] = \sum_{m=1}^{N} [L]_m^{\mathrm{T}} [k]_m [L]_m \tag{22}$$

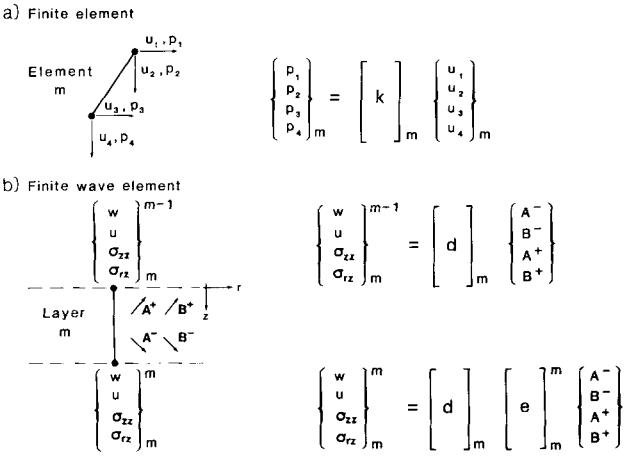

Figure 2. Analogy to finite element method. (a) Finite element with four degrees of freedom. (b) Finite wave element with four degrees of freedom.

and $\{R\}$ is the global force vector

$$\{R\} = \sum_{m=1}^{N} [L]_m^{\mathrm{T}} \begin{Bmatrix} r_1 \\ r_2 \\ r_3 \\ r_4 \end{Bmatrix}_m . \tag{23}$$

The vector $\{r_1, r_2, r_3, r_4\}$ represents the external forces acting on element number m, again concentrated at the nodes.

It is beyond the scope of the present paper to go into details concerning the actual implementation, but it is important to note the structure of the global systems of equations (21). As the topology matrices contain only zeros and ones, the matrix multiplications never need to be performed, but can be replaced by a set of indices (pointers) indicating the row and column of the global stiffness matrix where each element of the local ones have to be added. The actual generation of the global stiffness matrix can therefore be performed very efficiently once the local ones have been determined.

Returning to the determination of the depth-dependent Green's function in stratified media, the fact that the horizontal range dependence has been removed yields the possibility of effectively representing each layer as a 1-D 'finite wave element', as shown in Fig. 2(b), in formal analogy to standard finite elements as discussed above. The degrees of freedom for this element are here simply the wave amplitudes A_m^-, A_m^+, B_m^- and B_m^+, and these are conveniently collected in a local degree-of-freedom vector $\{a(k)\}_m$,

$$\{a(k)\}_m = \begin{Bmatrix} A_m^-(k) \\ A_m^+(k) \\ B_m^-(k) \\ B_m^+(k) \end{Bmatrix}, \quad m = 1, 2 \ldots N \tag{24}$$

where the subscript refers to the layer number. If the kernels for the field parameters involved in the boundary conditions, (9)–(12), are expressed in vector form as

$$\{v(k, z)\}_m = \begin{Bmatrix} w(k, z) \\ u(k, z) \\ \sigma_{zz}(k, z) \\ \sigma_{rz}(k, z) \end{Bmatrix}_m , \quad m = 1, 2 \ldots N \tag{25}$$

the following matrix relation is obtained for the homogeneous part of the solution

$$\{v(k, z)\}_m = [c(k, z)]_m \{a(k)\}_m, \quad m = 1, 2 \ldots N. \tag{26}$$

The matrix $[c(k, z)]_m$ is a function of horizontal wavenumber and z. As the depth dependence is present in the exponentials only, this matrix can be factorized as

$$[c(k, z)]_m = [d(k)]_m [e(k, z)]_m, \quad m = 1, 2 \ldots N \tag{27}$$

where $[d(k)]_m$ is a depth-dependent matrix containing only simple functions of k, and $[e(k, z)]_m$ is a diagonal matrix containing the exponentials.

The following expressions are now obtained for the field parameters from the homogeneous solution at the interfaces $m - 1$ and m, above and below layer m, respectively

$$\{v(k)\}_m^{m-1} = [d(k)]_m \{a(k)\}_m, \quad m = 2, 3 \ldots N \tag{28}$$

and

$$\{v(k)\}_m^m = [d(k)]_m \, [e(k)]_m^m \, \{a(k)\}_m, \quad m = 1, 2. \ldots N-1 \tag{29}$$

where the depth coordinate z has been removed and replaced by superscripts identifying the interfaces. For convenience the upper interface $m-1$ has been chosen as the origin of a local coordinate system making the exponential matrix $[e(k)]_m^{m-1}$ the identity matrix. We will return later to this specific choice in relation to numerical stability.

The field parameters in (28) and (29) are now superimposed with the corresponding forcing terms due to the sources within layer m to yield the total wavefield. The continuity of the superimposed field parameters at interface m can then be expressed as

$$\{v(k)\}_m^m + \{\overset{*}{v}(k)\}_m^m = \{v(k)\}_{m+1}^m + \{\overset{*}{v}(k)\}_{m+1}^m, \quad m = 1, 2. \ldots N-1 \tag{30}$$

where $\{\overset{*}{v}(k)\}_m^m$ and $\{\overset{*}{v}(k)\}_{m+1}^m$ are the source contributions arising from the sources in layer numbers m and $m+1$, respectively. If (30) is rewritten as

$$\{v(k)\}_m^m - \{v(k)\}_{m+1}^m = \{\overset{*}{v}(k)\}_{m+1}^m - \{\overset{*}{v}(k)\}_m^m, \quad m = 1, 2. \ldots N-1 \tag{31}$$

it expresses the cancellation of the discontinuity in the source fields by the discontinuity in the homogeneous solution. The interface discontinuity vector $\{v(k)\}^m$ is therefore introduced as

$$\{v(k)\}^m = \{v(k)\}_m^m - \{v(k)\}_{m+1}^m, \quad m = 1, 2. \ldots N-1 \tag{32}$$

and similarly for the source field discontinuity $\{\overset{*}{v}(k)\}^m$.

In order to assemble the local equations (31) into a global system, the global degree of freedom vector $\{A(k)\}$ in the up- and downgoing wavefield amplitudes is first introduced, defined by the unique local to global mapping

$$\{a(k)\}_m = [S]_m \, \{A(k)\}, \quad m = 1, 2. \ldots N. \tag{33}$$

After insertion of (28), (29) and (33), the discontinuity vector (32) takes the form

$$\{v(k)\}^m = ([d(k)]_m \, [e(k)]_m^m [S]_m - [d(k)]_{m+1} \, [S]_{m+1}) \, \{A(k)\},$$
$$m = 1, 2. \ldots N-1. \tag{34}$$

We now introduce a second unique mapping, collecting the local field discontinuity vectors $\{v(k)\}^m$ into one global discontinuity vector $\{V(k)\}$

$$\{V(k)\} = \sum_{m=1}^{N-1} [T]^m \, \{v(k)\}^m \tag{35}$$

which after insertion of (34) becomes

$$\{V(k)\} = \sum_{m=1}^{N-1} [T]^m \, ([d(k)]_m [e(k)]_m^m [S]_m - [d(k)]_{m+1} \, [S]_{m+1}) \, \{A(k)\}. \tag{36}$$

Similarly the global source field discontinuity vector $\{\overset{*}{V}(k)\}$ is

$$\{\overset{*}{V}(k)\} = \sum_{m=1}^{N-1} [T]^m \, (\{\overset{*}{v}(k)\}_m^m - \{\overset{*}{v}(k)\}_{m+1}^m). \tag{37}$$

The global cancellation of (36) by (37) therefore requires the following linear system of equations to be satisfied

$$[C(k)]\ \{A(k)\} = -\{\overset{*}{V}(k)\} \tag{38}$$

where $[C(k)]$ is the global coefficient matrix

$$[C(k)] = \sum_{m=1}^{N-1} [T]^m ([d(k)]_m [e(k)]_m^m [S]_m - [d(k)]_{m+1} [S]_{m+1}). \tag{39}$$

As can be observed, the global system (38) is very similar to the finite element system (21). The mapping matrices $[T]^m$ and $[S]_m$ are equivalent to the topology matrices $[L]_m$ defined for the finite element method in (20). However, due to the fact that the governing boundary conditions for the wave equation are not set up in the unknowns directly, but in derived quantities, two sets of topology matrices are needed here, one for the local-global mapping of the degrees of freedom, i.e. the wavefield amplitudes, and one for the physical field parameters involved in the boundary conditions.

The matrices $[S]_m$ and $[T]^m$ are extremely sparse, containing only zeros and ones. Since the mappings of (33) and (35) are unique, the corresponding summations and matrix multiplications in (37) and (39) need never actually be performed but can be replaced by a unique set of pointers, connecting the elements of the local systems with those of the global system, as illustrated in Fig. 3. As is the case in FEM programs, the topology matrices are therefore never set up in the actual computer code. Their formal use in (37) and (39) is, however, very convenient in the general fluid/solid/vacuum case, as the topology matrix $[S]_m$ is set up to include only the non-vanishing wavefield amplitudes and $[T]^m$ involves only the actual local boundary conditions, thus reducing the total number of equations and unknowns compared to the pure solid case.

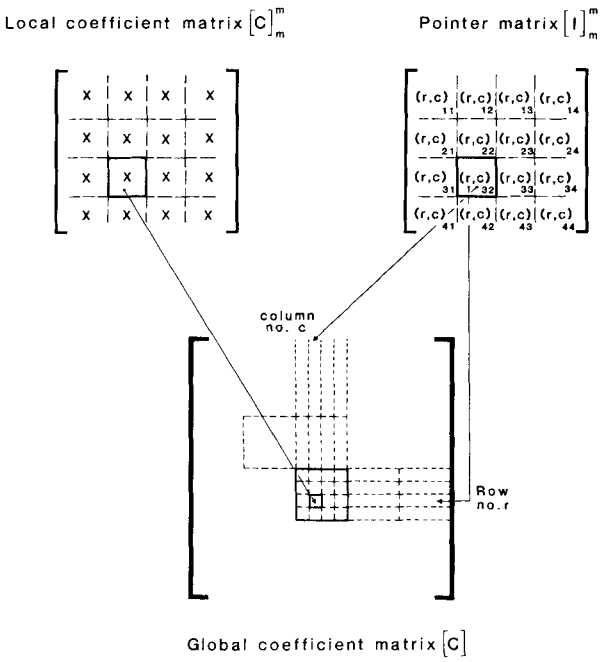

Figure 3. Mapping between local and global coefficient matrices by means of row and column pointers.

The pointer indices defined by the mappings of (33) and (35) depend solely on the number of unknowns within each layer and the boundary conditions at each interface, and can hence be determined *a priori*.

In this notation, the set-up of the global coefficient matrix requires only calculation of the elements of the matrices $[d(k)]_m$, which are very simple functions of the horizontal wavenumber, and the exponentials in $[e(k)]_m^m$, followed by the indexed move, illustrated in Fig. 3. The subsequent solution then yields the field in all layers simultaneously.

Although the global system of equations (38) is analytically well conditioned, apart from poles corresponding to normal modes and interface waves, its numerical solution is not necessarily stable. It is however possible to ensure unconditionally stable solutions by using Gaussian elimination with partial pivoting, where only simple scaling and rearrangement is employed. A detailed description is given by Schmidt & Jensen (1985) and only an outline will be given here.

The difference in absolute dimension between the displacement and stresses can yield a difference of several orders of magnitude between the coefficients in the corresponding rows for both local and global systems. As is well known in such cases, simple Gaussian elimination, with or without partial pivoting, will not guarantee unconditional numeric stability. In the present scheme, the equations for displacement and stress are therefore scaled in order to make all coefficients physically dimensionless.

Although from a theoretical point of view the origin of the local layer coordinate system can be chosen arbitrarily, its choice is quite critical for numerical stability when large real arguments of the exponential functions appear. This occurs for thick layers and large values of the horizontal wavenumber. However, for purely imaginary arguments the moduli of the exponential functions are unity. For real arguments (the evanescent regime), large differences in the order of magnitude of the exponential functions can occur. In this case, the resulting differences appear within the rows and thus row-scaling as before is inapplicable. Scaling could in principle be applied to the columns (via defactorization of growing exponentials; Chin *et al.* 1984) but, as shown by Schmidt & Jensen (1985), such scaling is in fact unnecessary when Gaussian elimination with partial pivoting is used to solve the global system. By choosing the origin of the local coordinate system at the uppermost boundary of the layer, and by arranging the mapping (33) such that the growing exponentials appear closest to the diagonal of the global system, Gaussian elimination with partial pivoting will automatically ensure that the wavefield amplitudes corresponding to the growing exponentials will be identically zero for large real arguments, in direct agreement with the physics of the waveguide problem, and thus yield numerically stable solutions.

The fact that no special numerical efforts except pivoting are needed to ensure unconditional numerical stability is believed to be the major reason for the computational efficiency of the SAFARI code.

Another important advantage of the present technique is that most operations, because of their potentially high degree of parallelism, can be easily vectorized for array-processor implementation. For example, since the local coefficient matrices (28) and (29) are similar for all layers, calculations of these, including the square roots and exponential functions, can be readily vectorized. In addition, the indexed move operations of the mappings are carried out with high efficiency on an array processor, and the same is the case for Gaussian elimination, which is intrinsically a sequence of vector operations. In the SAFARI code a combined envelope/band solver is used, taking optimal advantage of the block bi-diagonal structure of the global coefficient matrix.

When the global system of equations (38) has been solved, the kernels in (9)–(12) and (15)–(18) can readily be evaluated at any depth, the only additional functions needed being

the exponential functions of $[e(k, z)]_m$ in (27), all other functions having been evaluated while setting up the local coefficient matrices. The present technique is therefore highly efficient in cases where the total wavefield is to be determined at many depths, e.g. synthetic vertical seismic profiling (VSP).

The wavenumbers at which the depth-dependent Green's functions have to be determined are of course controlled by the numerical integration technique used for evaluation of the inverse transforms. Here the approximate scheme traditionally used in seismology is applied, e.g. Fuchs & Mueller (1971). First the Bessel functions are expressed in terms of Hankel functions, and the incoming contribution is neglected. Then the remaining Hankel function is replaced by its large argument approximation and the resulting integral is evaluated by means of a simple trapezoidal rule integration. When the Hankel transforms have been evaluated, the synthetic seismograms are straightforwardly generated by means of an FFT. In the examples presented in the following realistic attenuation is included in the layers, and a standard real axis integration is applied. It should, however, be stressed, that any complex integration contour could be chosen for both inverse transforms without any change of the basic Green's function algorithm. Any more accurate integration scheme could also straightforwardly be adapted to the global solution technique. The asymptotic Hankel transform used here gives significant errors only at very short ranges and steep propagation angles which, however, can be important in very short offset VSP modelling. For such cases the full Hankel transform algorithm of Tsang *et al.* (1974) or the recently developed fast Hankel transform, Anderson (1984), could be applied. For some long-range propagation problems, the wavenumber sampling could be significantly reduced by applying a Filon integration scheme, as per Frazer & Gettrust (1984). However, in the full solution (including all multiples) yielded by the present technique, the kernels are often highly oscillatory and analytic integration of the exponential function in the Hankel transform approximation therefore does not yield the same savings as in the reflectivity approximation outlined in the following section.

3.2 REFLECTIVITY APPROXIMATION

Due to the completeness of the present solution technique, all arrivals, including surface waves and trapped modes, are determined if the integration interval is chosen to be sufficiently large. As seismic sources are generally placed at or near the surface, these arrivals will usually dominate experimental seismograms, and thus also in synthetic seismograms obtained by a full wavefield model. In many areas of seismic work, these arrivals are, however, of limited interest, and it is therefore desirable to avoid them entirely in the synthetic seismogram computations. One such example is the investigation of reflected arrivals from deep crustal layers, e.g. MOHO and LVL models (Fuchs 1969; Braile & Smith 1975). Here, only body waves in the upper layers are desired. Due to the trigonometric relation between the angles of incidence and horizontal wavenumber, the integration interval can readily be chosen so that only these waves are included in the solution. It is well known, however, (Kennett 1983) that abrupt truncation of the integration interval can give rise to artificial numerical arrivals. These can be diminished by appropriately choosing the truncation points and by applying tapering at the ends of the actual integration interval. In this way, all multiple reflections within the shallow layers, and the surface influence on the source radiation pattern are retained in the DGM solution.

Another possibility is to apply the well-known reflectivity approximation of Fuchs & Mueller (1971) or Kennett (1974). The principle here is to divide the environment into a shallow refraction zone and a deep reflection zone. In the refraction zone, conical *P*-waves

:e propagated through the layers accounting only for transmission coefficients at the interaces. At the interface defining the subsequent reflectivity zone *P*-wave amplitudes are multiplied by the full reflection coefficient, and the resulting upgoing *P*-wave is now propagated back to the surface/borehole receivers. The single conical wave contributions are then superimposed by integration. As only real angles of incidence onto the reflectivity zone are of interest here (Aki & Richards 1980; Kennett 1983), this angle is conveniently used as integration variable, and the following integral representation for the surface displacements is obtained (Fuchs & Mueller 1971)

$$w(r, \omega)_m = C(\omega) \int_0^{\pi/2} \sin\theta \cos\theta \, H(\theta, \omega) R_{PP}(\theta, \omega) J_0(k_{pm} r \sin\theta) \, d\theta \tag{40}$$

where $C(\omega)$ is a function of frequency alone, $H(\theta, \omega)$ is a function of incident angle and frequency, accounting for the transmission through the refraction zone, and $R_{PP}(\theta, \omega)$ is the frequency-dependent *PP* reflection coefficient. The main body of calculations needed here is related to the determination of these reflection coefficients.

As was the case for the Green's function, the reflection coefficients have traditionally been determined by means of propagator matrices, as was done by Fuchs & Mueller (1971), or by the invariant embedding reformulation of Kennett (1974). However, since the solutions obtained by the present global technique are themselves the amplitudes of up- and downgoing conical waves, the reflection coefficients are easily obtained using the DGM solution method. If the refraction zone is replaced by a homogeneous half-space, and a compressional source is placed just above the interface, the kernels of (5) and (13) directly yield the following expression for the reflection coefficients

$$R_{PP}(\theta, \omega) = \alpha(k_{p1} \sin\theta) A_1^+(k_{p1} \sin\theta) \tag{41}$$

where A_1^+ is extracted from the global solution of (38).

An alternative reflectivity model has been readily developed as a natural outcome of the DGM approach. Some of the differences between the reflectivity model and the full wavefield solution will be demonstrated by numerical examples in the following sections.

4 Numerical examples

In the following, a series of propagation problems from both crustal and exploration seismology are treated in order to demonstrate the completeness, efficiency and versatility of the present solution technique.

First, canonical MOHO and LVL problems are considered for comparison with earlier results obtained by Braile & Smith (1975) using a reflectivity algorithm. These relatively simple problems are well suited to demonstrate the differences between the complete solution obtainable by the SAFARI DGM algorithm and the reflectivity approximation excluding refraction zone multiples and conversions.

As stated above, numerical stability is generally problematic for reflectivity algorithms in cases where the field in an intermediate layer becomes evanescent. In a second example, a simple canonical crustal model is modified by including a high-velocity layer, giving rise to wave-tunnelling. In such cases correct treatment of the evanescent regime is essential.

One of the most important features of the direct global approach is the efficient determination of the field at many receiver depths. This obviously makes it well suited for generation of synthetic vertical seismic profiles (VSP). As a third example a few test cases have been chosen in order to illustrate the synthetic VSP modelling capabilities of

SAFARI, not only for actual exploration or crustal applications, but also for improved interpretation of surface-received seismic records through purely hypothetical borehole seismology.

Finally, the generality and completeness of the present solution technique yields the possibility of modelling the propagation of the so-called inhomogeneous S^* and P^*-waves arising from sources close to a free surface or an internal velocity discontinuity. These waves are not predicted by geometrical ray theory; moreover, most earlier reflectivity models prevent analysis of these waves due to restrictions concerning source positions. Some recent results obtained by Hron & Mikhailenko (1981) using a finite difference approach, are reproduced here. Of equal interest, however, are the inhomogeneous arrivals, which in principle should be observable in seismic records obtained from earthquake sources in the vicinity of the MOHO, as predicted by Červený, Kozak & Pšenčik (1971). The SAFARI code has been used here to analyse the significance of these arrivals in seismic surface records for a simplified canonical crustal environment.

In all synthetic seismograms presented, the vertical particle velocity has been chosen as a representative field parameter. A simple N-shaped source pulse has been used, and calculations have been performed over a frequency band sufficiently wide to avoid numerical 'ringing' in the synthetic seismograms. The wavenumber interval used is stated for each example. The environmental parameters are selected from reported values. Velocity profiles are given, together with the synthetic seismograms, whereas the P-wave attenuations applied correspond to approximately $Q = 100$ in the shallow layers and $Q = 500$ in the deeper crust and the mantle. Where not stated, the shear velocities correspond to a Poisson's ratio of 0.25, while the shear attenuations have been chosen to correspond to $Q = 50$ and 250 for the shallow and deep regions, respectively.

The calculation times given in the following are for an FPS164 array processor. An estimate of the CPU requirements on, for example, a VAX 11/780, can be obtained by multiplying the stated numbers by 10.

4.1 MOHO TRANSITION AND LVL ZONES

During the past 20 years discussion has repeatedly focused on the detailed structure of the Mohorovičić discontinuity or crust–mantle transition beneath the continents. In many early crustal models (e.g. Pakiser 1963, 1985) the MOHO was represented as an abrupt transition corresponding to a simple velocity discontinuity. Later, however, experimental data and improved numerical modelling abilities have led to a representation of the crust–mantle transition as an extended gradient zone (Fuchs 1969; Meisnner 1973; review by Hale & Thompson 1982). It is outside the scope of the present paper to contribute to this discussion, but the significant number of numerical results presented in the literature makes these problems a convenient basis for comparison between the traditional numerical solution techniques and the present global approach.

As a first example, the simple MOHO-1 crustal model of Braile & Smith (1975) is chosen. The crust is represented by a single layer with $c = 6400$ m s^{-1} overlying the mantle in which $c = 8000$ m s^{-1}. The MOHO is here a simple velocity discontinuity at 30 km depth (Fig. 4a). An explosive source is placed at or close to the free surface, and the resulting N-shaped pulse is assumed to have maximum energy at 5 Hz. The frequency band is thus chosen to be 0–12.5 Hz in the calculations. Receivers are placed on the surface every 10 km out to 150 km range.

First, the resulting synthetic seismograms were computed by means of the SAFARI reflectivity approximation described above. All real angles of incidence were included, using

512 sample points in the angular integration, and a time window of 5 s width was chosen. The results are plotted in a standard stacked format with the amplitudes multiplied by the range in Fig. 4(b). The total calculation time was 40 CPU s on the FPS164, and the results are in total agreement with those given by Braile & Smith (1975).

The corresponding full wavefield solution is shown in Fig. 4(c). If the total wavenumber spectrum is included, it is obvious that surface waves would totally dominate the seismo-

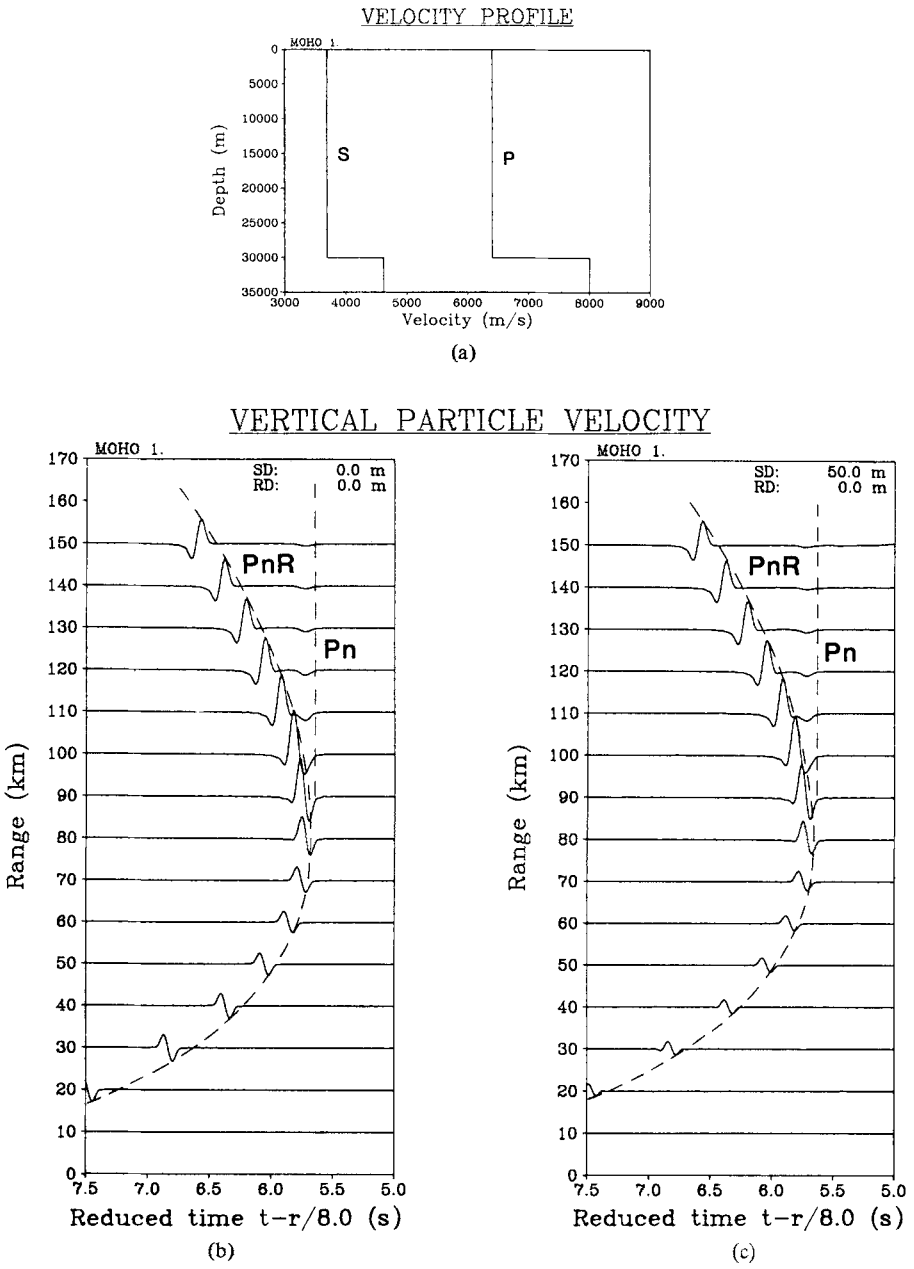

Figure 4. Synthetic seismograms for MOHO-1 crustal model. (a) Velocity profile. (b) Reflectivity approximation. (c) Full wavefield solution. Amplitudes are multiplied by range.

grams, as the source is only a small fraction of a wavelength away from the free surface, here 50 m. The wavenumber or slowness interval was therefore truncated to include only phase velocities between 5000 m s^{-1} and infinity, and the in-built Hermite polynomial tapering was applied to avoid artificial arrivals. As all multiples are included in the full solution it was necessary here to use a time window of 20 s width in order to avoid aliasing. Calculation time was 250 CPU s, again corresponding to 512 sample points in the wavenumber space. As expected for this very simple case, the agreement with the reflectivity results is almost total. Only at very short ranges do differences appear. These are due to the influence of the free surface on the source radiation pattern which, unlike the reflectivity approximation, the full solution automatically models.

It is well known that the more probable MOHO transition in many continental areas involves at least one velocity gradient and, as shown by Braile & Smith (1975), this characteristically gives rise to interference head waves. In order to analyse this phenomenon and at the same time demonstrate the use of purely hypothetical vertical seismic profiles (VSP) for interpretational purposes, synthetic VSPs were generated for the MOHO-5 model of Braile & Smith (1975) (Fig. 5a). Receivers are assumed to be positioned at 100 km range in the depth interval of 25–35 km with a vertical spacing of 1 km. Again 512 wavenumber samples were used, with an integration interval from 4100 m s^{-1} to infinity in horizontal phase velocity, and a time window of 20s. The synthetic VSP is shown in Fig. 5(b). The first arrival is the *Pn* head wave. Its interference nature is clearly observable from the behaviour in the gradient zone between 30 and 35 km depth. In this type of synthetic record, other arrivals above the MOHO are clearly identifiable as the direct *P*-wave, the *PP* reflection and a converted *PS* reflection. At the end of the time period shown, the same behaviour is observable for the first multiple. The total calculation time on the FPS164 was 15 min in this case.

The last crustal model treated here, the LVL-6 of Braile & Smith (1975), considers the influence of one or more low-velocity layers (LVL) in the Earth's upper crust. In contrast to the simple MOHO models above, recognition of a crustal LVL from seismic refraction data alone is extremely difficult, because all LVL-related phases are necessarily secondary arrivals and no refracted head wave from the uppermost LVL boundary is possible.

Again, both the reflectivity approximation and the full wavefield solution were determined for the crustal model shown in Fig. 6(a). In both cases only waves with angles of incidence of less than 35° on to the shallowest interface (2000 m) were included by appropriately truncating the integration intervals. This was done in order to exclude the supercritical reflections from this interface. The reflectivity result is shown in Fig. 6(b), and the agreement with Braile & Smith (1975) is again complete. The first arrival is the *Pg* head wave, observable mainly at subcritical ranges, followed by the *PlR* reflection from the upper LVL at large ranges. In addition, *PcR* multiply-reflected phases can be observed as secondary arrivals and, at longer ranges, the *Pc* interference head wave from the lower crust is significant. The same properties characterize the full solution shown in Fig. 6(c). Here, however, *PgS* and *PcS* arrivals clearly appear in association with the *Pg* and the *Pc* arrivals, respectively. These 'ghost arrivals' are due to *P*–*S* conversion at the 2000 m interface, and their significance in the synthetic seismograms clearly demonstrates the importance of the additional information obtainable from the full solution. It should be noted that the seismograms in Fig. 6(c) were obtained for the case in which the free surface was removed and the uppermost layer replaced by a half-space, in order to avoid the shallow multiples and surface waves, which were not considered in previous reflectivity calculations.

The seismograms in Figs 6(b) and 6(c) were obtained in 7 min on the FPS164 using 512 wavenumber samples and a 10 s time window.

4.2 SEISMIC TUNNELLING WAVES

As stated above, the numerical stability in the evanescent regime has traditionally been a difficult problem for models of the present integral transform type. To demonstrate the numerically stable behaviour of the present solution technique in such cases, we next consider the so-called wave-tunnelling phenomenon variously described by Fuchs & Schultz (1976) and Menke & Richards (1980). The tunnelling effect arises in a crust characterized by a 'double duct' velocity profile, i.e. two low-velocity zones separated by a relatively thin high-velocity layer. For angles of incidence larger than critical, the *P*-waves inside this layer

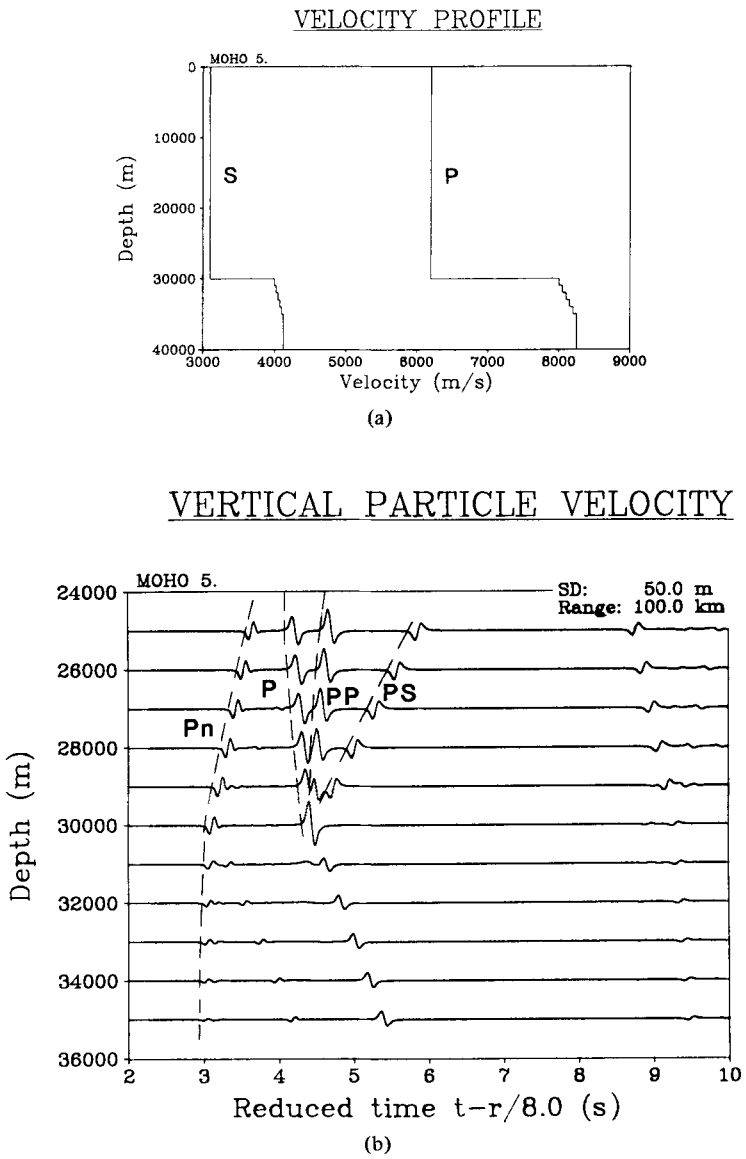

Figure 5. Synthetic seismograms for MOHO-5 crustal model. (a) Velocity profile. (b) Synthetic VSP at 100 km range and 25–35 km depth.

will be evanescent. The penetration depth of the 'exponential tails' will, however, increase with decreasing frequency, and at low frequencies the amplitude will be finite at the lower boundary. Energy will therefore leak into the lower duct, where propagation will continue at supercritical angles. The lower duct now acts as a wave tunnel in which these waves are trapped, but for each interaction with the high-velocity layer some energy will obviously leak back into the upper duct, giving rise to additional arrivals at supercritical ranges. Due to the evanescent behaviour in the intervening layer, these arrivals are not predicted by geometrical ray theory. For high frequencies their amplitude will vanish at the lower boundary, and the layer will work exactly like an infinite half-space for the *P*-waves. This behaviour characterizes a numerically stable solution.

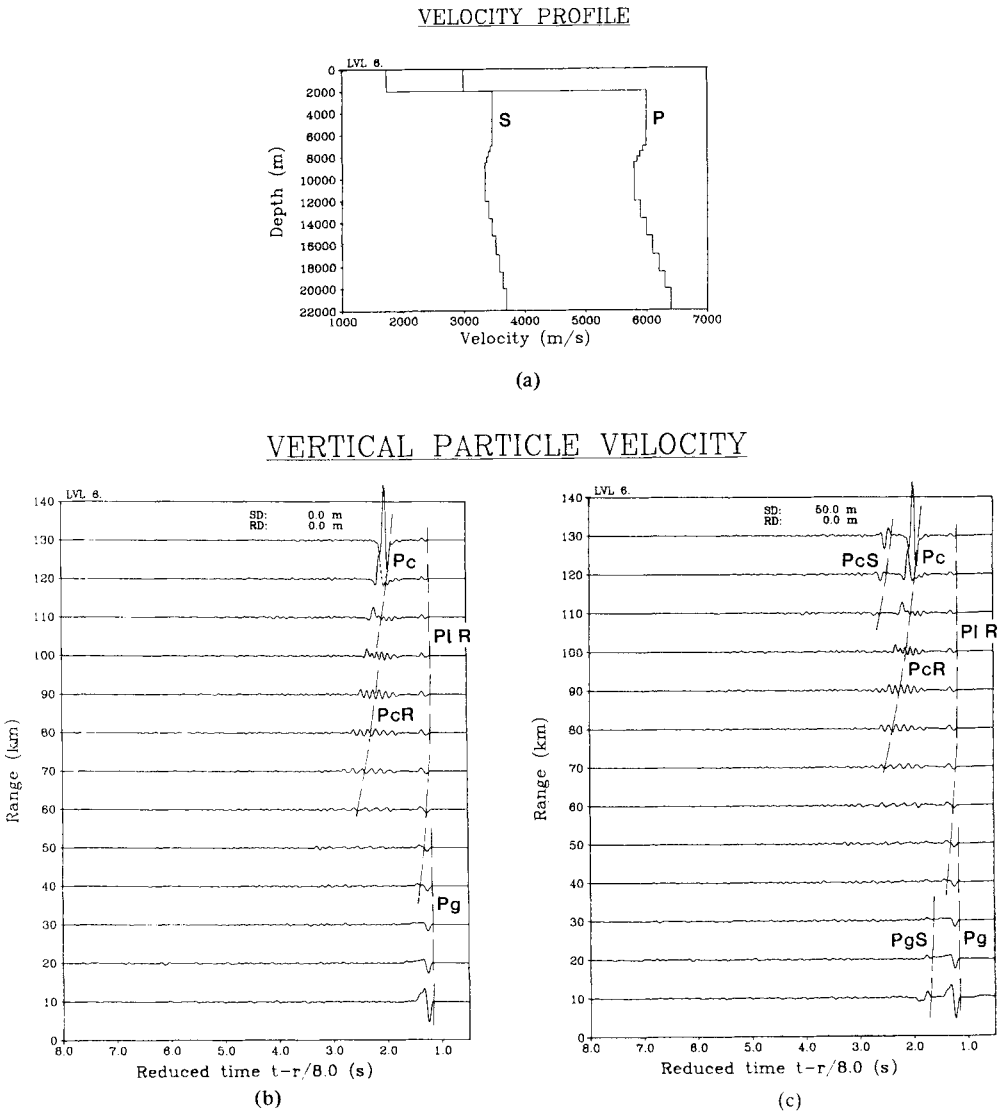

Figure 6. Synthetic seismograms for LVL-6 crustal model. (a) Velocity profile. (b) Reflectivity approximation. (c) Full wavefield solution. Amplitudes are multiplied by range.

To underscore the tunnelling phenomenon specifically, a very simple crustal model is chosen for this study. It is basically the MOHO-1 model presented above, but modified to include a thin layer at 25 km depth with the properties of the mantle. In the first example (Fig. 7), the thickness of the layer is 1 km. Using the same source properties and receiver geometry as in the MOHO-1 case, the seismograms in Fig. 7(b) were obtained. The first arrival is the direct *P*-wave followed by the *PhR* reflection from the high-velocity layer. A corresponding *Ph* head wave is not observable due to the relatively small thickness of the layer. A weaker *PnR* reflection from the MOHO then follows. Finally, tunnel waves are

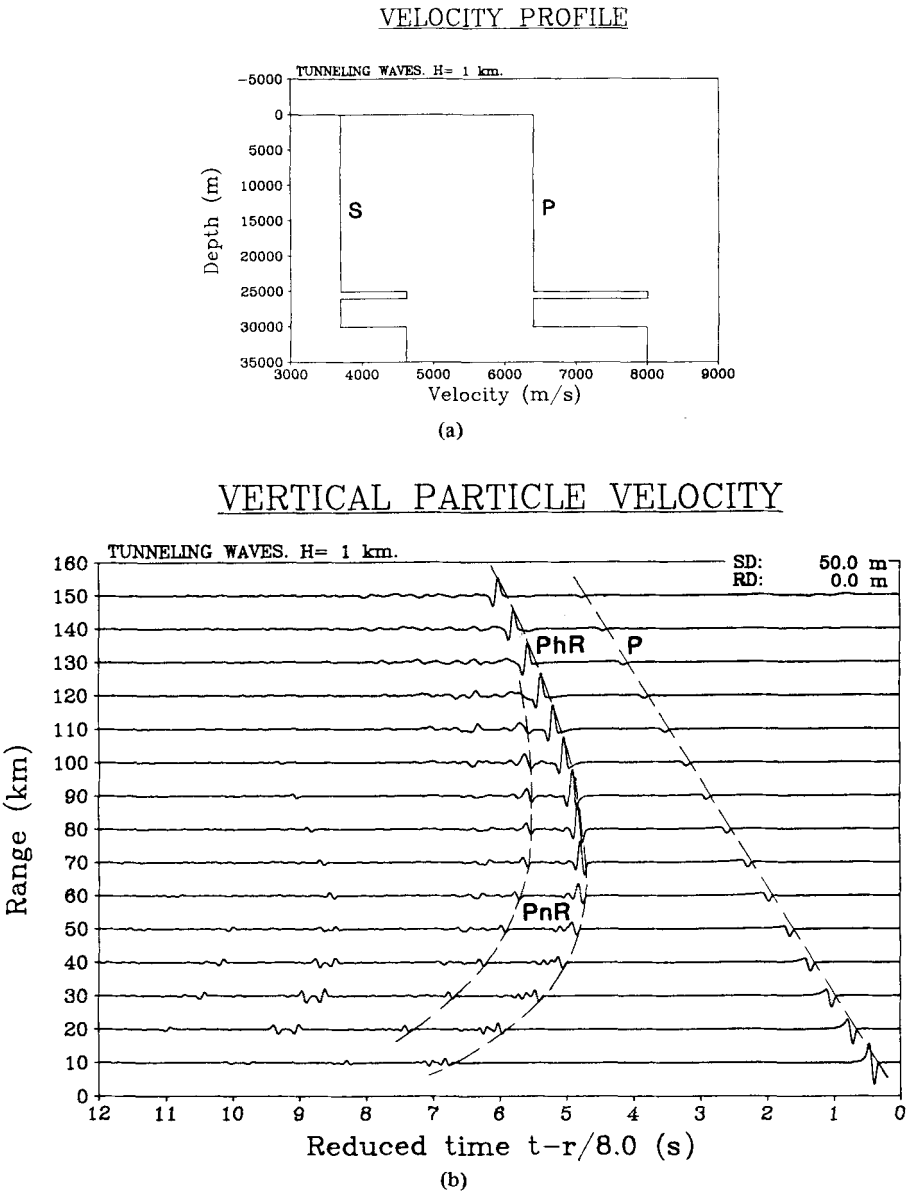

Figure 7. Tunnelling waves for 1 km high-velocity layer. (a) Velocity profile. (b) Synthetic surface seismograms. Amplitudes are multiplied by range.

observable at supercritical ranges, but their amplitudes are insignificant. The thickness of the layer was therefore reduced to 200 m. The resulting seismograms (Fig. 8) reflect the same basic properties as before but, as expected, the *PnR* reflection is more pronounced and even the *Pn* head wave is observable. The multiples due to tunnelling are now clearly observable at supercritical ranges, with the characteristic increasing shadow zone for increasing order of the multiple. The later arrivals at subcritical ranges are in both cases converted shear modes.

No artificial high-frequency noise is present in the seismograms of Figs 7 and 8, indicating the numerical stability of the present solution technique at higher frequencies. Using a time window of 40 s and 512 sampling points in the wavenumber integration, the seismograms were obtained in 12 min on the FPS164.

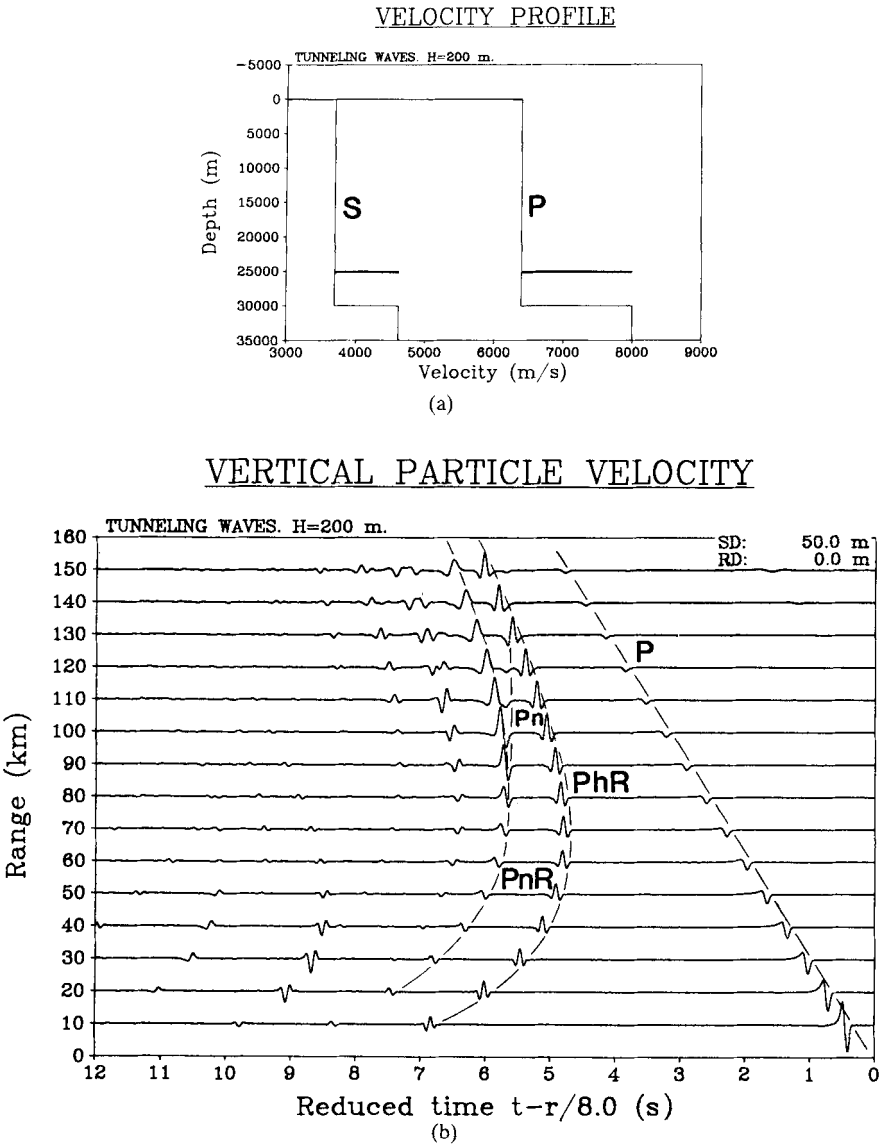

Figure 8. Tunnelling waves for 0.2 km high-velocity layer. (a) Velocity profile. (b) Synthetic surface seismograms. Amplitudes are multiplied by range.

4.3 VERTICAL SEISMIC PROFILING

In recent years there has been a growing recognition of the important additional information obtainable from vertical seismic profiling (VSP), not only for exploration, but also for deep crustal seismology (Stephen 1977; Stephen, Louden & Matthews 1980; Hardage 1983; Balch 1984). In principle, the VSP technique, as developed by Gal'perin (1973), is based on the positioning of an appropriate number of receivers in a borehole. By displaying the recorded seismograms in a depth-stacked format an intuitive 'ray' picture results, effectively decomposing the wavefield into up- and downgoing contributions. These can then graphically be associated with primary and multiple reflections, refractions, and mode conversions. In addition to the extensive planning and cost involved in borehole seismology, the absence of widely applicable numerical tools for synthetic VSP generation has obstructed the widespread use of this powerful technique. In recent years a number of numerical methods for this purpose have therefore arisen, based, for example, on classical or generalized ray methods (Ursin 1982), discrete wavenumber (Bouchon & Aki 1977; Dietrich & Bouchon, 1985) and reflectivity techniques (Temme & Mueller 1982; Stephen 1977). However, these techniques have in general been either approximate or extremely expensive in terms of calculation time.

The present solution technique is, due to its global nature and generality, directly suited to efficient computation of synthetic VSP. In addition to the example of purely hypothetical VSP already shown, two examples will be given here for realistic problems in both crustal and exploration seismology, to demonstrate this important feature of the global solution technique. A more detailed analysis is given by Tango (1985).

The first example shows how synthetic VSP can be used in the planning of actual VSP experiments. The simple ocean-crust model shown in Fig. 9(a) was used by Stephen *et al.* (1980) in the design of the Oblique Seismic Experiment (OSE) for DSDP boreholes. Here we use the SAFARI code for a preliminary analysis of the influence of source offset on the resolution of VSPs obtained in a marine crustal environment.

To obtain exact solutions, even at zero offset, the calculations are performed in plane geometry, including the negative wavenumber spectrum corresponding to incoming waves. For simplity of interpretation, the ocean is represented by a fluid half-space and an explosive source with peak energy at 10 Hz is assumed to be placed 200 m above the sea bed. The receivers, 11 in total, are placed in a borehole between 6000 and 7000 m depth. Using 1024 samples, the wavenumber integration is performed over a symmetric interval corresponding to angles of incidence less than 43° on to the sea bed, removing complicating surface wave contributions. The calculation was performed over a 0–25 Hz frequency interval in steps of 0.2 Hz, corresponding to a 5 s time window. Since each additional source offset only requires extra integrations at very minor CPU cost, 10 offsets were treated in one solution pass, with a total calculation time of 8 min. Three characteristic examples are shown in Fig. 9(b), corresponding to offsets of 1, 3 and 5 km. The VSP for the smallest offset is seen to be dominated by downgoing wavetrains, but the significance of upgoing contributions increases with increasing offset. It was found that an offset of 3–4 km yields an optimal combination of up- and downgoing contributions.

The next example concerns a coal-seam stratigraphy in the Ruhr district used by Temme & Mueller (1982) to evaluate their purely acoustic VSP model. For comparison, the results of Temme & Mueller are first reproduced for a selected offset. Shear properties are then considered in all layers, to demonstrate the importance of including mode conversions in this type of calculation. The compressional velocity profile is shown in Fig. 10(a). The source, at 5 m depth, is assumed to have peak energy at 50 Hz, and a 0–150 Hz frequency band was chosen. The acoustic VSP for a source offset of 500 m is shown in Fig. 10(b), and, in agree-

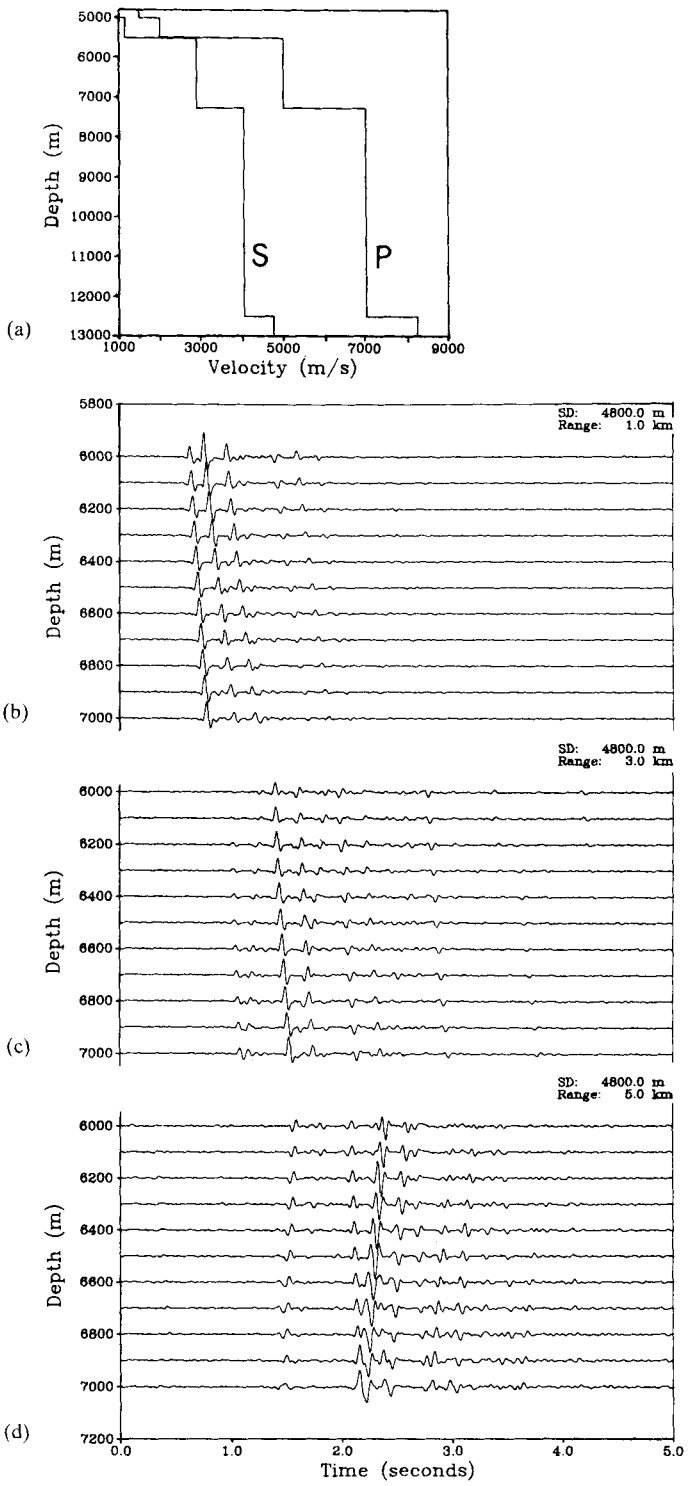

Figure 9. Synthetic VSPs for OSE crustal model. (a) Velocity profile. Source offsets: (b) 1 km, (c) 3 km, (d) 5 km.

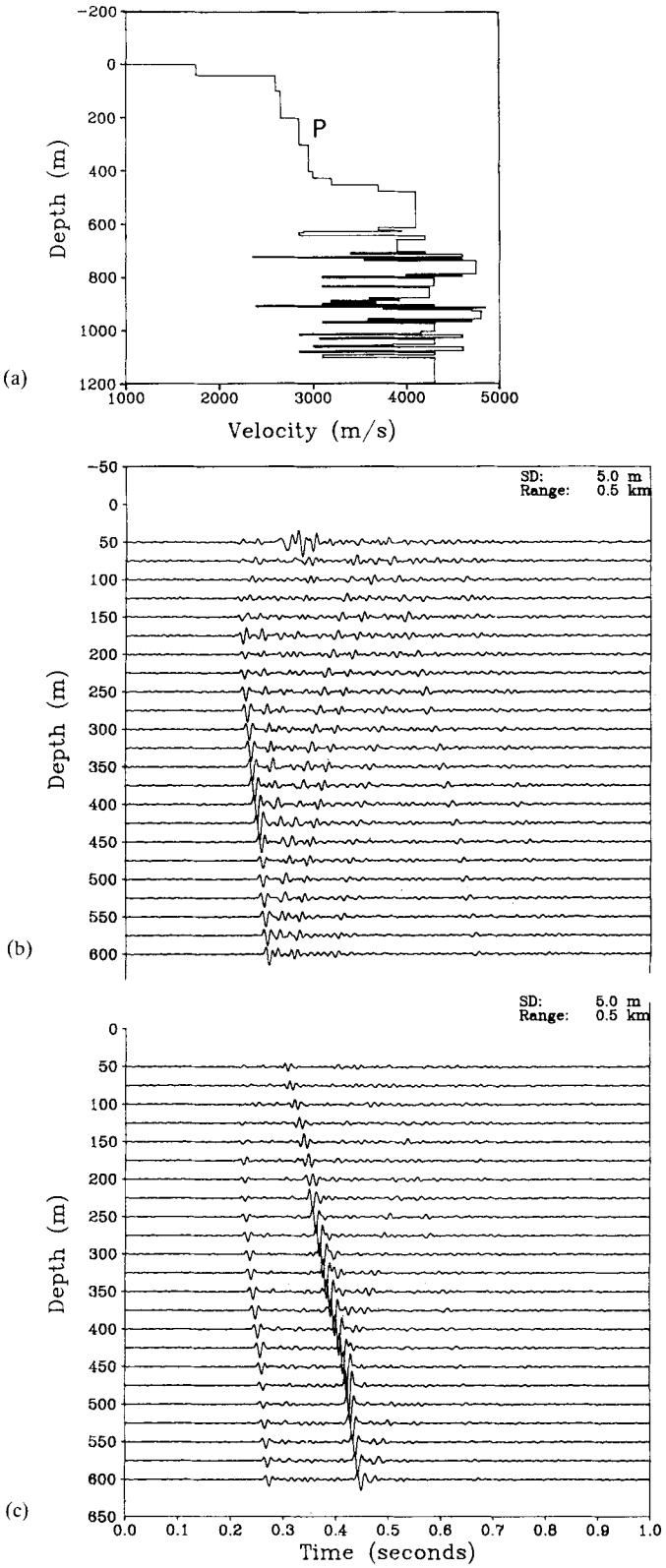

Figure 10. Synthetic VSPs for coal-seam stratigraphy. (a) Velocity profile. (b) Acoustic VSP. (c) Seismic VSP.

ment with the results presented by Temme & Mueller, both up- and downgoing waves are clearly observable. In the elastic case, however, a converted shear wave clearly dominates the downgoing wavefield, and thus obscures interpretation of weak reflections from the deeper layers (Fig. 10c). The converted shear modes were found to be significant for offsets in excess of 300 m for the present case, again illustrating the importance of using synthetic VSP in the planning of VSP experiments. The efficiency of the SAFARI algorithm is especially evident in this multi-offset case, where the environmental model contains more than 50 layers. The acoustic and seismic VSPs for five ranges were computed in 30 and 90 min, respectively, using a 2 s time window and 1024 wavenumber samples.

4.4 INHOMOGENEOUS S^* ARRIVALS

The completeness and generality of the present approach allows modelling the behaviour of the so-called inhomogeneous or pseudo-spherical S^*- and P^*-waves, which were 'discovered' by Červený *et al.* (1971) and more recently analysed by Hron & Mikhailenko (1981) and Gutowski *et al.* (1984) using a finite difference algorithm. These waves give rise to extra arrivals not predicted by geometric ray theory, apparently radiating from a point on a boundary of a large velocity contrast close to a buried point source. Inhomogeneous arrivals are characterized by an angle-dependent radiation pattern and their amplitude increases exponentially as the distance between the source and the interface decreases.

Although, from a ray-theory point of view, these waves are often called 'non-geometric' arrivals, their presence can be shown to be directly related to the curvature of the incident wavefield at the interface (Hron & Mikhailenko 1981) or, which is equivalent, to the significance of the evanescent part of the wavenumber spectrum of the incident source field. This is easily demonstrated by means of the same superposition principle basic to the present solution technique. As an example, we consider a source close to the free surface of an homogeneous half-space. The field produced at the free surface by the source is decomposed into conical waves by the Sommerfeld integral representation (13). For $k < k_{pm}$ the conical waves are homogeneous due to the imaginary argument of the exponential function. However, for $k > k_{pm}$, the argument becomes real and the waves are inhomogeneous or evanescent. The amplitude of the source field will therefore decrease exponentially for increasing source depth in this spectral regime. In order to satisfy the boundary conditions at the surface, the source field is superposed with the homogeneous solutions (5) and (6). In the spectral region $k_{pm} < k < k_{sm}$ the conical shear wave components are, however, homogeneous conical waves, while the compressional waves are inhomogeneous as stated above. It is therefore evident that some of the source-wave energy in this wavenumber interval will couple into homogeneous shear waves, the S^*-waves, and that their excitation will be exponentially decaying with source depth. In a similar way, the presence of both P^*- and S^*-waves in the case of sources close to internal interfaces (Červený *et al.* 1971) can be easily demonstrated. Here, we first reproduce some of the numerical experiments of Hron & Mikhailenko (1981) for exploration-type sources close to the surface of an homogeneous half-space. When the source and receiver positions are expressed in terms of wavelength the problem is dimensionless. Here we choose a half-space with a compressional velocity of 6000 m s^{-1} and a shear velocity of 3000 m s^{-1}, corresponding to a Poisson's ratio of 0.33. The usual N-shaped pulse with peak energy at 5 Hz is chosen for the source. The dominant compressional wavelength is then $\lambda = 1200$ m, which is therefore the basic unit of length. The source is placed $\lambda/8$, or 150 m, below the surface, and the synthetic seismograms are first determined as a function of range for a fixed depth of 3λ (Fig. 11). In addition to the 'geometric' *P*, *PP*, and *PS* arrivals, the S^* arrival is clearly observable. The results are in close

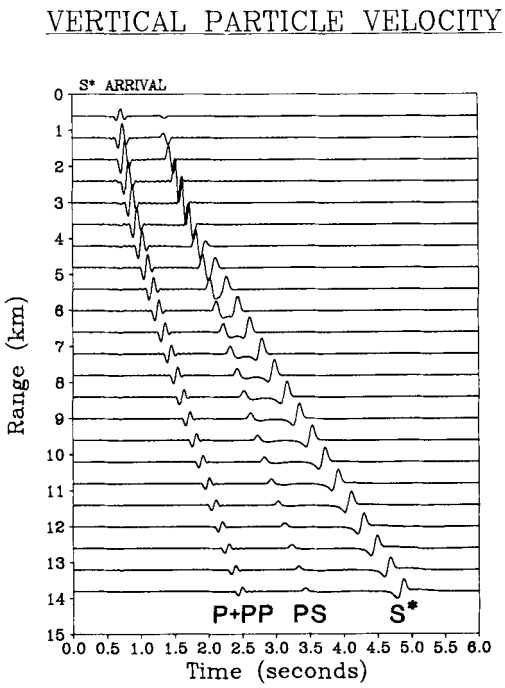

Figure 11. S^* arrivals for source $\lambda/8$ below the free surface. Receiver depth 3λ and ranges $0.5-11.5\ \lambda$ ($\lambda \approx 1200$ m). Amplitudes are multiplied by range.

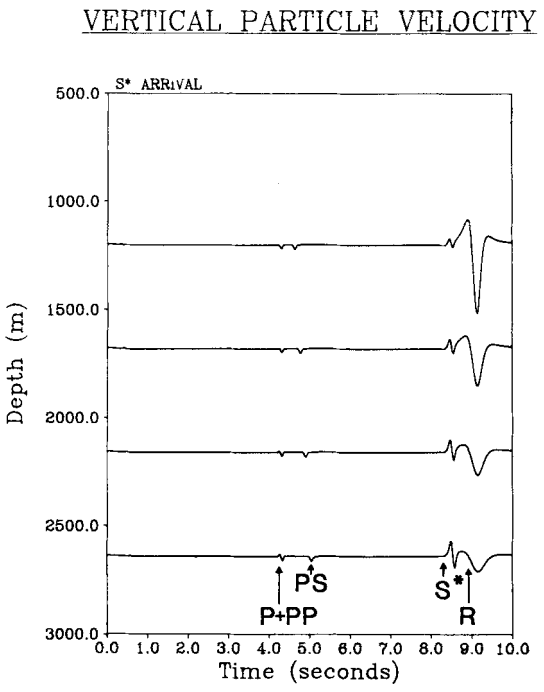

Figure 12. S^* arrivals for source $\lambda/8$ below free surface. Receiver range 21λ and depths $1.0-2.2\lambda$ ($\lambda = 1200$ m).

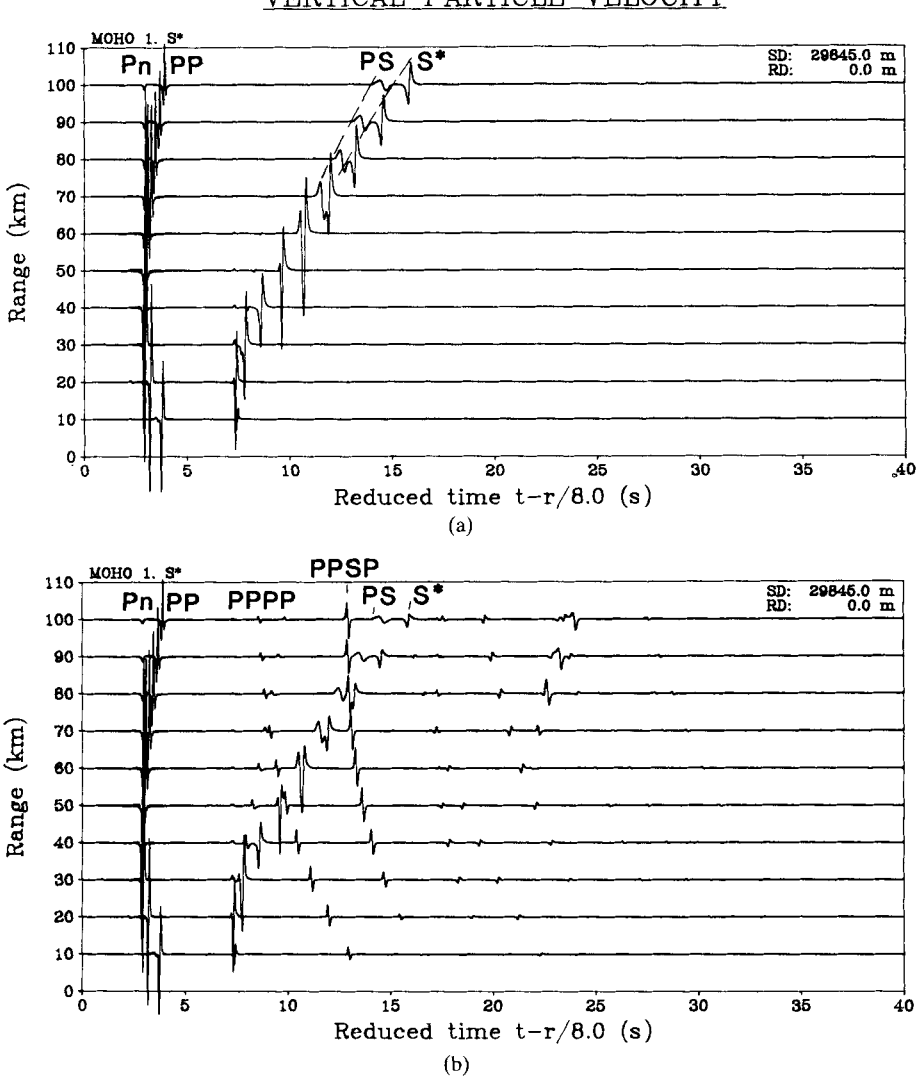

Figure 13. S^* arrivals for MOHO-1 crustal model with source $\lambda/8$ above the MOHO (λ = 1280 m). (a) Free surface removed. (b) Free surface present. Amplitudes are multiplied by range.

agreement with those obtained by Hron & Mikhailenko (1981) using, however, a narrower banded and thus more oscillatory pulse.

The seismograms shown in Fig. 12 are the corresponding responses at different receiver depths for a fixed range of 21λ. The shallowest receiver is at 1λ and the deepest at 2.2λ depth. The Rayleigh wave 'R' is significant at these shallow depths and its evanescent nature and the associated depth dispersion are clearly observable. This is in direct contrast to the behaviour of the S^* arrival, which has an increasing amplitude with depth and no significant depth dispersion, again in full agreement with Hron & Mikhailenko (1981). The seismograms in Figs 11 and 12 were obtained in 80 s on the FPS164 using 1024 wavenumber samples and a time window of 10 s.

Although surface-generated S^*-waves are also potentially important in relation to

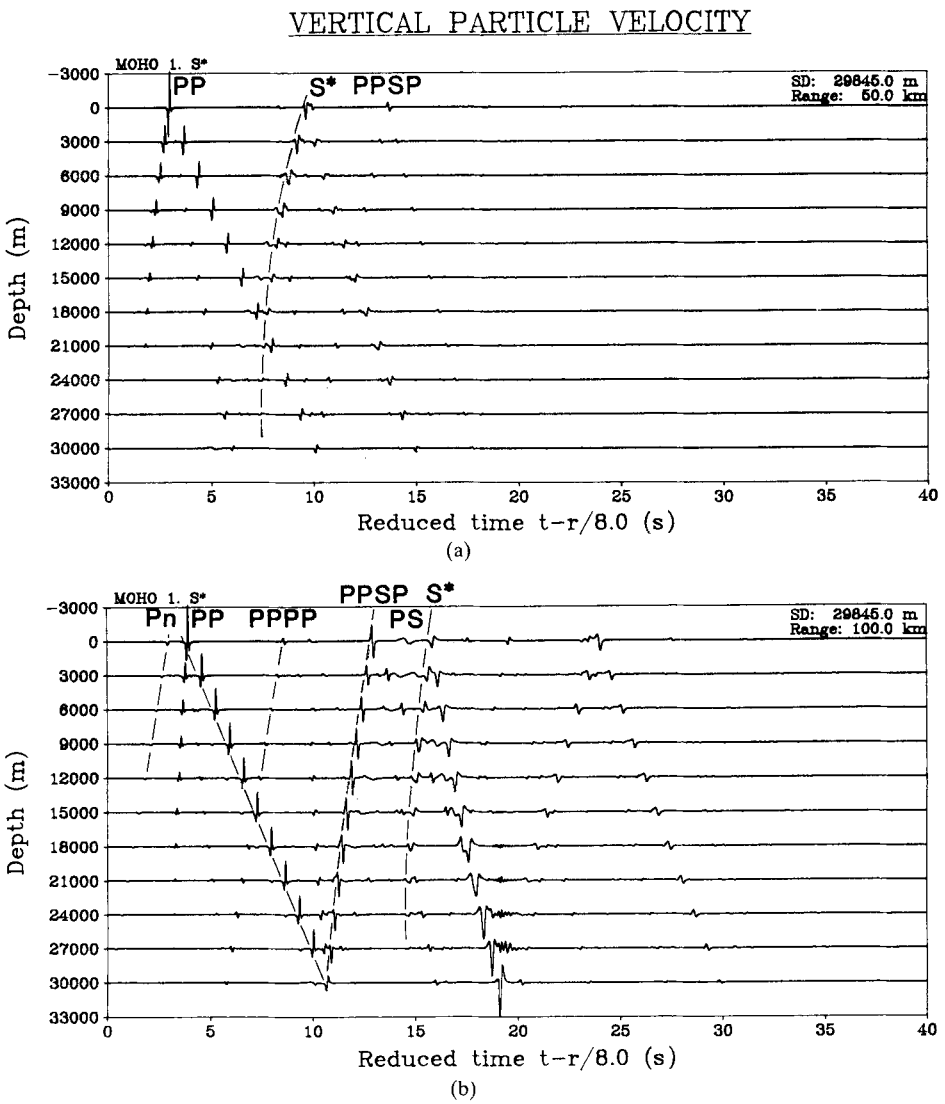

Figure 14. Hypothetical VSP for MOHO-1 crustal model with source λ/8 above the MOHO (λ = 1280 m). Ranges are (a) 50 km and (b) 100 km.

exploration and experimental crustal seismology, we next consider the behaviour and significance of the inhomogeneous waves that could, in principle, be generated by earthquakes close to the MOHO, as proposed by Červený *et al.* (1971).

We will again choose the simple MOHO-1 crustal model for this study, using the same calculation parameters as earlier, but now placing the compressional source 1/8λ of the dominant wavelength above the MOHO. Initially the free surface is removed in order to avoid multiples. The synthetic seismograms in Fig. 13(a) show the expected *Pn* headwave and the *PP* reflection, which arrives almost simultaneously with the direct *P*-wave. Then the converted *PS* arrival appears, followed by a significant S^* contribution, thus confirming Červený's *et al.* predictions. As in the half-space case above, the separation between the *PS* and the S^* arrivals increases with range. As a result of introducing the free surface (Fig.

13b), a significant number of multiples now obstructs a direct recognition of the S^* arrival. By comparison with Fig. 13(a) it is, however, still observable, although of lower relative amplitude due to the reflection process now included at the free surface. Again, hypothetical VSPs, as shown in Figs 14(a) and 14(b) for 50 and 100 km ranges, respectively, can be used as an additional interpretational tool, yielding immediate identification of the multiples in Fig. 13(b).

The seismograms of Figs 13(a) and 13(b) were obtained in 10 and 15 min respectively, whereas the VSPs in Fig. 14 required 30 min, all based on 1024 wavenumber samples and 40 s time window, corresponding to 500 samples in the actual 0–12.5 Hz frequency band.

5 Conclusions

A direct global matrix approach to the solution of the depth-separated wave equation in horizontally stratified environments has been presented. In addition to being numerically efficient, its global nature yields the possibility of treating problems with many receivers in depth with only one solution pass. Further, there are no restrictions on the number or type of sources that can be used, thereby allowing the determination of fields produced by phased source arrays. The numerical solutions are unconditionally stable for all combinations of sources, receivers, frequency and environment. The technique is entirely general, as there are no restrictions concerning the environmental layering. Mixed solid/fluid/vacuum cases are treated with a minimum of arithmetic operations. These features make the present DGM approach an efficient basis for a general computer code applicable to a large class of wave propagation problems, not only in the seismic field, as illustrated by the examples presented here, but also in underwater acoustics and ultrasonics.

References

Aki, K. & Richards, P., 1980. *Quantitative Seismology*, W. H. Freeman & Co., San Francisco.

Anderson, W. L., 1984. Computation of Green's tensor integrals for three-dimensional electromagnetic problems using fast Hankel transforms, *Geophysics*, **49**, 1754–1759.

Balch, A., 1984. *Vertical Seismic Profiling*, IHRDC Press, Boston.

Bouchon, M. & Aki, A., 1977. Discrete wavenumber representation of seismic source wave fields, *Bull. seism. Soc. Am.*, **67**, 259–277.

Braile, L. & Smith, R., 1975. Guide to the interpretation of crustal refraction profiles, *Geophys. J. R. astr. Soc.*, **40**, 145–176.

Červený, V., Kozak, J. & Pšenčík, I., 1971. Refraction of elastic waves into a medium of lower velocity – pseudospherical waves, *Pure appl. Geophys.*, **92**, 115–132.

Chapman, C. H. & Orcutt, J. A., 1985. The computation of body-wave synthetic seismograms, *Rev. Geophys. Space Phys.*, submitted.

Chin, R. C. Y., Hedstrom, G. W. & Thigpen, L., 1984. Matrix methods in synthetic seismograms, *Geophys. J. R. astr. Soc.*, **77**, 483–502.

Dietrich, M. & Bouchon, M., 1985. Synthetic vertical seismic profiles in elastic media, *Geophysics*, **50**, 224–234.

Ewing, W. M., Jardetzky, W. S. & Press, F., 1957. *Elastic Waves in Layered Media*, McGraw-Hill, New York.

Frazer, L. N. & Gettrust, J. F., 1984. On a generalization of Filon's method and the computation of the oscillatory integrals of seismology, *Geophys. J. R. astr. Soc.*, **76**, 461–481.

Fuchs, K., 1969. On the properties of deep crustal reflectors, *Z. Geophys.*, **35**, 133–149.

Fuchs, K. & Mueller, G., 1971. Computation of synthetic seismograms with the reflectivity method and comparison with observations, *Geophys. J. R. astr. Soc.*, **23**, 417–433.

Fuchs, K. & Schultz, K., 1976. Tunnelling of low frequency waves through the subcrustal lithosphere, *J. Geophys.*, **42**, 175–190.

Gal'perin, E. I., 1973. *Vertical Seismic Profiling*, Society of Exploration Geophysiscists, Tulsa.

Gutowski, P., Hron, F., Wagner, D. E. & Treitel, S., 1984. S^*, *Bull. seism. Soc. Am.*, **74**, 61–78.

Ha, J., 1984. Recurrence relations for computing *P* and *SV* seismograms, *Geophys. J. R. astr. Soc.*, **79**, 863–874.

Hale, L. & Thompson, G., 1982. The seismic reflexion character of the Mohorovicic discontinuity, *J. geophys. Res.*, **87**, 4625–4635.

Hardage, B. A., 1983. *Principles of VSP, Part A*, Geophysical Press, Amsterdam.

Harkrider, D. G., 1964. Surface waves in multilayered elastic media, part I: Rayleigh and Love waves from buried sources in a multilayered elastic halfspace, *Bull. seism. Soc. Am.*, **54**, 627–679.

Haskell, N. A., 1953. The dispersion of surface waves in multilayered media, *Bull. seism. Soc. Am.*, **43**, 17–34.

Hron, F. & Mikhailenko, G., 1981. Numerical modelling of nongeometrical effects by the Alekseev–Mikhailenko method, *Bull. seism. Soc. Am.*, **71**, 1011–1029.

Jardetzky, W. S., 1953. Period equation for an *N*-layered halfspace and some related questions, *Tech. Rep. Seism. No. 29.* Columbia University, Lamont, Geological Observatory.

Kennett, B. L. N., 1974. Reflections, rays, and reverberations, *Bull. seism. Soc. Am.*, **65**, 1685–1696.

Kennett, B. L. N., 1983. *Seismic Wave Propagation in Stratified Media*, Cambridge University Press.

Kind, R., 1976. Computation of reflection coefficients for layered media, *J. Geophys.*, **42**, 191–200.

Kind, R., 1978. The reflectivity method for a buried source, *J. Geophys.*, **44**, 603–612.

Krenk, S. & Schmidt, H., 1982. Elastic wave scattering by a circular crack, *Phil. Trans. R. Soc. A*, **308**, 167–198.

Kutschale, H., 1973. Rapid computation by wave theory of propagation loss in the Arctic Ocean, *Columbia Univ. Tech. Rep. Cu-8-73.*

Meisnner, R., 1973. The 'Moho' as a transition zone, *Geophys. Surv.*, **1**, 195–216.

Menke, W. H. & Richards, P. G., 1980. Crust–mantle whispering gallery phases: a deterministic model of teleseismic *Pn* wave propagation, *J. geophys. Res.*, **85**, 5416–5422.

Miklowitz, J., 1978. *The Theory of Elastic Waveguides*, North Holland Press, Amsterdam.

Pakiser, L. C., 1963. Structure of the crust and upper mantle in the western United States, *J. geophys. Res.*, **68**, 5747–5756.

Pakiser, L. C., 1985. Historical review of seismic exploration of the crust and upper mantle of the basin and range province, *Mem. geol. Soc. Am.*, submitted.

Pekeris, C. L., 1948. Theory of propagation of explosive sound in shallow water, *Mem. geol. Soc. Am. No. 27.*

Schmidt, H., 1983. Excitation and propagation of interface waves in a stratified seabed, in *Acoustics and the Sea-Bed*, ed. Pace, P. C., Bath University Press.

Schmidt, H., 1984. Modelling of pulse propagation in layered media using a new fast-field program, in *Hybrid Formulation of Wave Propagation and Scattering*, ed. Felsen, L. B., Martinus Nijhoff Publishers, The Hague.

Schmidt, H. & Jensen, F. B., 1984. An efficient numerical solution technique for wave propagation in horizontally stratified ocean environments, *SM-173*, SACLANT ASW Research Centre.

Schmidt, H. & Jensen, F. B., 1985. A full wave solution for propagation in multilayered viscoelastic media with application to Gaussian beam reflection at fluid/solid interfaces, *J. acoust. Soc. Am.*, **77**, 813–825.

Stephen, R. A., 1977. Synthetic seismograms for the case of the receiver within the reflectivity zone, *Geophys. J. R. astr. Soc.*, **51**, 169–181.

Stephen, R. A., Louden, K. E. & Matthews, D. H., 1980. The oblique seismic experiment on DSDP Leg 52, *Geophys. J. R. astr. Soc.*, **60**, 289–300.

Tango, G. J., 1985. Applications of a direct fast field/reflectivity program to wave propagation modeling in underwater acoustics and solid earth seismic environments, *MSc thesis*, University of New Orleans.

Temme, P. & Mueller, G., 1982. Numerical simulation of vertical seismic profiling, *J. Geophys.*, **50**, 177–188.

Thomson, W. T., 1950. Transmission of elastic waves through a stratified solid, *J. appl. Phys.*, **21**, 89–93.

Tsang, L., Brown, R., Kong, J. A. & Simmons, G., 1974. Numerical evaluation of electromagnetic fields due to dipole antennas, *J. geophys. Res.*, **79**, 2077–2080.

Ursin, B., 1982. Computation of zero offset vertical seismic profiles, *SINTEF Rep. STF 28 A83011*, Tronheim, Norway.

Woodhouse, J. H., 1981. Efficient and stable methods for performing seismic calculations in stratified media, in *Physics of the Earth's Interior*, eds Dziewonski, A. & Boschi, E., Elsevier, New York.

Zienkiewitz, O. C., 1977. *The Finite Element Method*, 3rd edn, McGraw-Hill, London.